Date: January 20th, 2026
Submitted to: Water Research

Enabling microbial electrolysis cell scale-up via electrochemistry-, hydrodynamic-, and microbial ecology-informed framework

Danbee Kim[a], Nakyeong Yun[a], Hongang Du[a], Cheng Li[b], Sarah Preheim[a], Ruggero Rossi[a*]

[a] Department of Environmental Health and Engineering, Whiting School of Engineering, Johns Hopkins University, Baltimore, MD 21218, USA

[b] Department of Biological & Ecological Engineering, Oregon State University, Corvallis, OR 97331, USA

* Corresponding authors: Ruggero Rossi (rrossi4@jh.edu)

Abstract

Microbial electrolysis cells (MECs) can produce green hydrogen while removing organic contaminants from liquid waste streams by leveraging the metabolic activity of electroactive microorganisms. Despite their potential in a sustainable, circular economy, large-scale MECs that can treat relevant volumes of wastewater have failed to deliver performance proportional to their lab-scale counterparts. The reason behind this lower performance at scale remains unclear. In this study, we developed a combined electrochemistry-, hydrodynamic-, and microbial ecology-informed framework to analyze and optimize MEC performance during scale-up, enabling accurate quantification of major limitations and the identification of strategies to overcome them, ultimately facilitating equivalent performance at scale. Applying this framework to the scale up of a zero-gap MEC from 9 cm^2 electrode area to 100 cm^2 electrode area, resulted in similar maximum current densities in a 100 cm^2 MEC (21.7 ± 1.1 A/m^2) compared to a 9 cm^2 system (25.1 ± 2.7 A/m^2), as well as equivalent hydrogen production rates of 69.3 L/L-d (100 cm^2) and 67.7 ± 2.4 L/L-d (9 cm^2). COMSOL flow dynamics simulations were used to scale up the reactor configuration without negatively affecting electrolyte velocity and distribution in the cell, minimizing the increase in internal resistances during scale up (11.7 ± 0.5 $m\Omega m^2$ at 9 cm^2; 19.7 ± 1.3 $m\Omega m^2$ at 100 cm^2). Microbial community structures were assessed at both scales using high-throughput sequencing, highlighting the

similarity of populations across electrode dimensions and operational parameters. The framework presented here accelerates the development of effective strategies toward the scale-up of MECs by furthering the understanding of how electrochemical, hydrodynamic, and microbial ecology parameters change as the reactor dimension is increased. Ultimately, this approach contributes to advancing electrochemical biotechnology toward practical deployment in energy-efficient wastewater treatment systems.

Keywords: scale-up, microbial electrolysis cell, zero-gap MEC, hydrogen production rate, flow path

Introduction

Microbial electrolysis cells (MECs) can produce hydrogen gas from liquid waste streams while removing organic contaminants from solution. By coupling wastewater treatment with hydrogen production, MECs can reduce the strain on the wastewater infrastructure and return clean water to the environment while fulfilling a portion of the growing demand for hydrogen gas for chemicals, fertilizers, and energy production. In MECs, the anode is colonized by electroactive bacteria that oxidize the organic matter in solution and produce electrons (Lee et al., 2022). These electrons are consumed at the cathode, where the water is reduced to hydrogen gas. A relatively low voltage (0.1 based on thermodynamics; 0.6–1.0 V in operational conditions) is required to drive hydrogen production in MECs compared to the 1.4–1.8 V needed for abiotic water electrolysis (Kim et al., 2025). In addition, by leveraging electroactive microorganisms on the anode, MECs can operate with impaired electrolytes with variable composition, while conventional abiotic electrolyzers require ultrapure water or concentrated corrosive solutions (Ghorui et al., 2024). However, in MECs, the rate of hydrogen production relies on microbial metabolism, which can be several orders of magnitude lower than the typical hydrogen production rates of abiotic electrolyzers. Therefore, engineering efforts are needed to scale up MECs and achieve relevant hydrogen productivity while treating large volumes of wastewater.

Large-scale MECs have been designed and operated, but larger systems have always produced lower current density and, therefore, lower hydrogen production rates compared to their small-scale counterparts (Jiang et al., 2025). Despite the several examples of bench

and pilot-scale reactors available in the literature, it is not yet clear what primarily contributes to lower performance at scale. This lack of understanding arises from the interaction between multiple factors that change concurrently during scale-up, including electrochemical, microbial, and hydrodynamic attributes of large reactors. Electrochemical performance, such as anode and cathode resistances, is influenced by the electrode size (Fan et al., 2008; Rossi et al., 2019a). The carbonaceous electrodes typically used as anodes can have a large electrical resistance, contributing to high current losses in larger electrodes. For example, it was previously reported that a carbon mesh anode resistance increased up to three times when the electrode dimension was increased from 10 cm^2 to 1 m^2 (Cheng et al., 2014). The microbial community has been shown to change from small-scale to large-scale MECs, which in turn can affect the efficiency of organic matter degradation or current production (San-Martín et al., 2019). Different hydrodynamic characteristics at scale can cause changes in flow patterns and mass transfer, which can alter biofilm formation and activity, increase the likelihood of clogging or mass-transport limited regimes, and consequently impact performance (Gao et al., 2021; Kim et al., 2025). Therefore, changes in electrochemical, microbial, and hydrodynamic characteristics of MECs during scale-up led to changes in performance in larger reactors. While previous studies recognized that electrochemical, microbial, and hydrodynamic characteristics of MECs dictate performance, these attributes have never been examined and controlled simultaneously during scale-up, leading to confusion regarding their relative contribution to current and hydrogen production rate, and to a lack of strategies to regulate these attributes during scale-up. Enabling the development of large-scale MECs with performance proportional to smaller systems requires comprehensive exploration and regulation of the electrochemical, microbial, and hydrodynamic features of MECs while scaling-up.

In this study we track the electrochemical, hydrodynamic, and microbial community attributes of a zero-gap MEC while scaling-up the electrode area by one order of magnitude, from 9 cm^2 to 100 cm^2. Whole cell internal resistance, anode, cathode, and ohmic resistances were monitored via the electrode potential slope analysis and electrochemical impedance spectroscopy, allowing us to understand and control the electrochemical performance during scale-up. Microbial community analysis via 16S rRNA gene sequencing was employed to compare the similarity of microbial populations across different anode dimensions, while fluid

dynamics simulations were used to estimate differences in flow velocities and electrolyte distribution. By developing a framework to monitor and understand MEC features during scale-up, this work provides an approach that can be used in future studies to guide the development of larger reactors by minimizing major performance limitations and thereby advancing the practical application of MECs.

Materials and Methods

2.1. Zero-gap MEC configurations

One 100 cm^2 MEC and two 9 cm^2 MECs were assembled with two PVC end plates (196 cm^2 for 100 cm^2 cell and 36 cm^2 for 9 cm^2 cells) with a threaded insert to allow liquid flow into the cell (Figure 1; Figure S1). The serpentine flow paths facilitate electrolyte flow and optimize liquid distribution across the electrode in both anode and cathode chambers, as previously demonstrated (Kim et al., 2025). The 100 cm^2 MEC was designed to ensure uniform flow distribution and minimize electrochemical losses, with key geometric considerations optimized for high-performance operation (Sauermoser et al., 2020) (Figure 1A). The 100 cm^2 MEC incorporated five parallel serpentine channels of equal length, while the 9 cm^2 MEC used a single serpentine channel. A reduced channel aspect ratio (0.5, equation 1) was maintained in both MECs to increase the anolyte inlet flow velocity, enhance liquid water removal, and promote ion transport in both MECs (Sauermoser et al., 2020). The utilization of shorter multiple channels in the 100 cm^2 cell lowered the overall pressure drop and enhanced flow uniformity across the electrode surface, compared to a single long-channel configuration. A length-to-width ratio (equation 2; 14 for 9 cm^2; 47 for 100 cm^2 MEC) greater than 1 improved the mechanical stability of the flow field according to previous studies.

$$\text{Channel aspect ratio} = D/W \quad \text{(equation 1)}$$

$$\text{Length-to-width ratio} = L/W \quad \text{(equation 2)}$$

where D is the channel depth, W is the channel width, and L is the channel length.

The electrode packing density (anode area/anode volume) was 286 m^2/m^3 for 9 cm^2 and 100 cm^2 MECs. Furthermore, the Reynolds numbers (equation 3) of the 9 cm^2 was 9.8, similar to that of the 100 cm^2 MEC, which was 12. Therefore, a similar laminar flow regime was maintained during the scale-up.

$$\text{Reynolds number} = \rho u D_h/\mu \quad \text{(equation 3)}$$

where ρ is fluid density (kg/m^3), u is average fluid velocity (m/s), D_h is hydraulic diameter (m), and μ is dynamic viscosity (Pa·s).

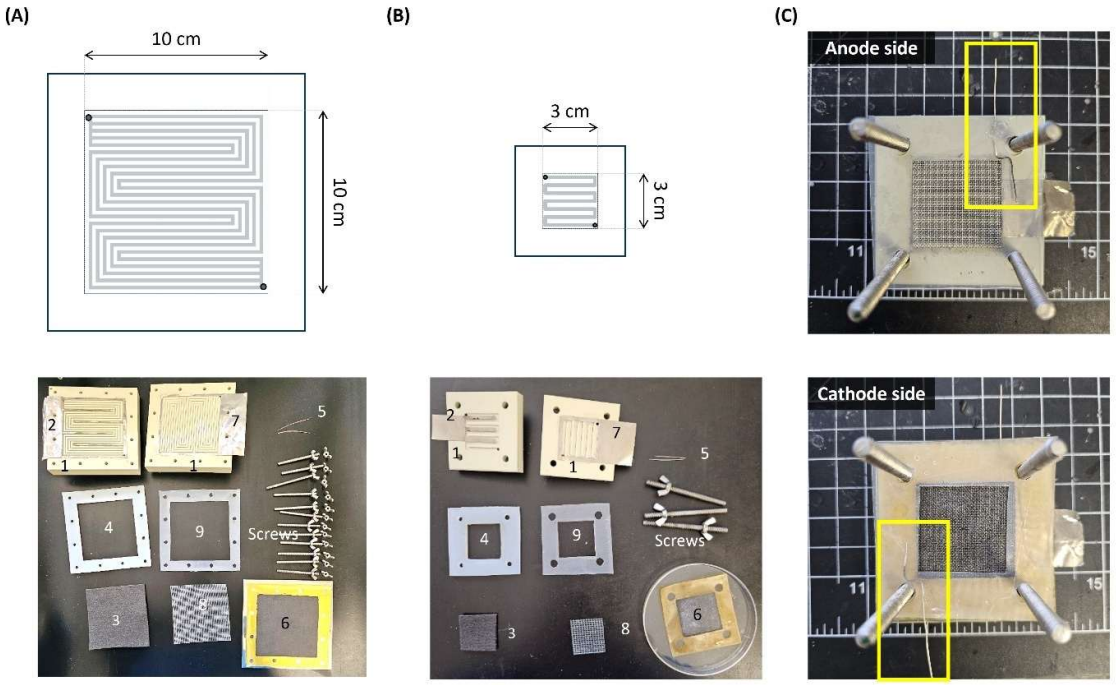

Figure 1. Schematic of the flow-field design of (A) 100 cm^2 and (B) 9 cm^2 MECs with serpentine flow field. (1) end plate, (2) anode current collector, (3) carbon felt anode, (4) 3 mm silicon gasket for anode chamber, (5) Ag/AgCl wires for pseudo-reference electrode, (6) membrane electrode assembly (MEA), (7) cathode current collector, (8) plastic spacer, (9) 0.5 mm silicon gasket. (C) Photograph of pseudo-reference electrodes (pRE) used to monitor anode and cathode performance positioned inside the reactor in contact with the membrane.

Compressible silicon gaskets with a thickness of 3 mm for the anode chamber and 0.5 mm for the cathode chamber were used to achieve a zero-gap configuration with no spacing between electrodes and the AEM. In this configuration, the hydroxide ions generated at the cathode are selectively transported to the anode, enabling larger current densities and hydrogen production rates (Rossi et al., 2022). Stainless steel wire cloth (SUS 304, 50 x 50 Mesh, McMaster-Carr) was used as an anode in the abiotic test. A carbon felt anode (3.18 mm thick, Alfa Aesar) was used for the biotic test and was heat-treated at 450 °C for 30 minutes prior to use to increase the electrochemical surface area (Feng et al., 2010). Anode and cathode chambers were separated by a 130 μm-thick AEM (Fumasep FAA-3-PK-130, Fuel Cell

Store). The cathode membrane electrode assembly (MEA) was obtained by hot pressing (70 °C) the AEM and cathode at 0.1 MPa for 3 min (Park et al., 2019). The AEM was pretreated by soaking in 1 M NaOH for 24 h prior to use, following the manufacturer's instructions. The NiMo catalyst used for the cathode was synthesized as previously described (Rossi et al., 2023a) and was sprayed onto a bare, wet-proofed carbon cloth (5% PTFE; Fuel Cell Store) with a final loading of 3 mg/cm^2, then dried overnight at ambient conditions before assembling into the MEA (Kim et al., 2025).

Titanium foils (Strem Chemicals Inc.) were used as anode and cathode current collectors. The anode current collectors were comb-patterned to avoid interference with flow distribution, while the cathode current collectors had square-shaped perforations. Pseudo-reference electrodes (pRE), which were Ag/AgCl wires, were used to continuously monitor anode and cathode potentials during operations. The Ag/AgCl wires were installed in contact with the membrane but outside the electric field in both the anode and cathode chambers and maintained in place during assembly with the silicon gaskets (Figure 1E). Conventional reference electrodes could not be directly inserted into the zero-gap cell due to the lack of space. An external Ag/AgCl reference electrode (BASi), was installed on the anode effluent tube to calibrate the pREs before starting the experiments (Figure S2). After the reactor was assembled with the pREs, the potential of the pREs was regularly calibrated using the external Ag/AgCl as a reference. External reference electrodes are affected by a large ohmic loss and, therefore, cannot be used to monitor the electrode potential in zero-gap configurations (Hansen et al., 2022). Due to their placement close to the electrodes, pREs allowed continuous monitoring of the electrode potential in situ.

The hydrogen gas generated at the cathode was captured in gas bags (Calibrated Instrument Inc.) connected with the cathode chamber and analyzed with a gas chromatograph (SRI Instrument) equipped with a molecular sieve column. No catholyte was used in the MECs to prevent competition in the migration of anions other than hydroxide ions from anode to cathode (Rossi et al., 2022). The water needed for the hydrogen evolution reaction at the cathode diffused through the AEM from the anode chamber as previously described (Rossi et al., 2023a). The hydrogen cost was calculated based on the industrial electricity price for 2023 in the U.S. reported by the EIA ($0.0804/kWh). The MEC energy consumption was estimated by multiplying the total Coulombs by V_{cell} and then converting the resulting energy from joules

to kilowatt-hours using the relative conversion factor (1 kWh=3.6 × 10^6 J). The energy consumption was then multiplied by the electricity rate to determine the total electricity cost. Finally, the total electricity cost was divided by the amount of hydrogen produced (in kilograms) to yield the cost of hydrogen in \$/kg H_2.

2.2. MEC operation

The MECs were fed with defined media or real single-stage anaerobic digestor effluents. The 500 mL of anolyte was continuously recirculated in both MECs with a retention time of 0.36 min unless otherwise noted. This retention time corresponds to 12 mL/min in the 9 cm^2 cell and 131 mL/min in the 100 cm^2 cell. Experimental conditions were set to match the equivalent hydraulic retention times (1.08 min, 0.54 min, 0.36 min, 0.27 min, and 0.22 min) used in a prior study for the 9 cm^2, so that the impact of the retention time can be compared between small and large MECs (Kim et al., 2025). The flow rates were adjusted to achieve the same retention time in both small and large MECs, allowing for a direct comparison of scale-up effects under equivalent hydrodynamic conditions (Kim et al., 2025). For the tests using a synthetic electrolyte, 50 mM phosphate buffer solution was used as an anolyte (PBS; 4.58 g/L Na_2HPO_4, 2.45 g/L $NaH_2PO_4 \cdot H_2O$, 0.31 g/L NH_4Cl, 0.13 g/L KCl; σ = 7 mS/cm) containing 2 g/L (9 cm^2) or 5 g/L (100 cm^2) sodium acetate with trace vitamin and mineral solution as previously described (Kim et al., 2025). Due to the rapid substrate consumption rate in the 100 cm^2 cell, the anolyte containing 5 g/L of sodium acetate was replaced daily, whereas the 9 cm^2 cells anolyte was replenished every two days (Table S1 and S3).

A single-stage anaerobic digester effluent was used to evaluate the performance of the 100 cm^2 MEC with real waste streams. The effluent was collected from the Sod Run wastewater treatment plant, MD, USA. The polarization test was conducted using the filtered effluent (20 μm filter paper, VWR) while long-term operation was evaluated using settled media. The effluent was stored at 4 °C prior to use for up to one week. The same effluent was used in a previous study in the 9 cm^2 configuration, enabling direct comparison of the impact of scale-up on MEC performance with real domestic waste streams. The MECs were operated at 35 °C. Inoculation was performed by adding 50 mL of effluent from other operating bioelectrochemical cells to the anolyte for the first five cycles, rather than by transferring an inoculated anode from other reactors as previously reported (Kim et al., 2025). The anolyte

was sparged with N_2 to remove residual dissolved oxygen from the solution for approximately 10 min prior to use.

2.3. Electrochemical analysis

Chronopotentiometry (CP) was used to investigate the performance of the cathodes using small and large electrodes in a current range from –300 mA to 0 mA for the 100 cm^2 electrode and from –27 mA to 0 mA for the 9 cm^2 electrode, corresponding to a current density range of 0 to 30 A/m^2 in 50 mM PBS to evaluate electrochemical performance. The biotic tests were carried out with an external voltage ranging from –0.6 V to –1.3 V, using the anode as working electrode and a power supply as the source (LW-K3010D, Longwei, China). In the 100 cm^2 MEC, a 1 Ω resistor was connected in series between the cell and the power supply to measure the voltage loss and calculate current density, while in the 9 cm^2 MECs, a 10 Ω resistor was used for the same purpose. The voltage measured across the resistor (V_{loss}) and the cell voltage (V_{cell}) were recorded every 20 minutes with a Keithley 2700. Ohm's law was used to calculate the current density (A/m^2) based on the voltage loss across the resistor, normalized by the MEC cross-sectional area.

The MEC performance was evaluated based on internal resistance and onset voltage using the electrode potential slope (EPS) method (Cario et al., 2019). This method estimates the internal resistance from the slope of the polarization curve and determines the onset potential (excluding activation losses) from the intercept at zero current on the linear region of the curve. Comparing internal resistance and onset potential between the different reactors allows us to assess the impact of the design and operational parameters on electrochemical performance. Anode and cathode resistances and onset potentials were estimated with the EPS analysis from the electrode potentials over the current density range selected for the polarization curve. Electrode and whole-cell resistances were compared with each other and with the solution resistance (R_Ω) across different MEC dimensions (9 cm^2 and 100 cm^2). The solution resistance was estimated as the high-frequency intercept of the Nyquist plot from the electrochemical impedance spectroscopy (EIS) analysis (from 500 kHz to 1 mHz, 10 mV amplitude, 10 points s^{-1}), measured in whole-cell mode.

2.4. COMSOL modeling for flow contour

The flow fields of two different MEC systems were analyzed using COMSOL Multiphysics 6.2 at five different retention times (0.22, 0.27, 0.36, 0.54, and 1.08 min) for both the 9 cm^2 and the 100 cm^2 MECs. Experimental conditions were set to match the equivalent hydraulic retention times used in a prior study for the 9 cm^2, so that the impact of the retention time can be compared between small and large MECs (Kim et al., 2025). Fluid flow within the system was simulated under steady-state conditions using the Single-Phase Laminar Flow module and the Porous Media and Subsurface Flow module based on the Brinkman equations, assuming the system was fully saturated with electrolyte. By comparing element sizes, a finer mesh was employed to accurately model the flow within the channels, electrodes, and their interfaces (Figure S3). Model parameters for the materials of the system were implemented using the same values as in the previous study (Kim et al., 2025). The uniformness of the flow field was quantified by calculating the coefficient of variation of the velocity distribution, defined as the ratio of the standard deviation to the mean velocity (Li, 2025). A lower coefficient of variation typically indicates a more uniform flow across the reaction area (Kim et al., 2021).

2.5. Microbial community analysis

To assess microbial community similarity across electrode dimensions and operational conditions, anodic biofilms were sampled from 9 sections of the 100 cm^2 cell and 4 sections of the 9 cm^2 cell after 144 days of operation with defined media. DNA samples were collected from each electrode area facing the membrane by scrubbing with autoclaved cotton-tipped applicators. The collected DNA samples were briefly stored at –4 °C in a freezer prior to shipment. The collected samples were sent to RTL Genomics (USA) for DNA extraction and library preparation using the 515F/806R EMP primers (PRK 515F: 5’-GTGCCAGCMGCCGCGGTAA-3’ and 806R: 5’-GGACTACHVGGGTWTCTAAT-3’), followed by paired-end sequencing on the Illumina MiSeq platform. Raw reads with low quality scores, ambiguous bases, or potential chimeric sequences were removed using the USEARCH fastq filter function (Edgar, 2010). The remaining high-quality reads were clustered into operational taxonomic units (OTUs) using the UPARSE algorithm, and the obtained OTUs were taxonomically classified against the UNOISE SINTAX algorithm (Edgar, 2016). Positive and

negative controls were included in the microbial community analysis (Figure S4). The negative control, consisting of the autoclaved cotton-tipped applicator, did not yield any detectable sequences, confirming the absence of contamination. Correlation analysis and diversity index were performed using PAST software (version 5.2.1) (Hammer and Harper, 2001), based on Pearson's correlation coefficient (*r*). The sequence data generated in this study were deposited in the NCBI Sequence Read Archive under the Bioproject accession number PRJNA1314789.

2.6. Analytical methods

The volume of hydrogen gas produced was measured as previously described (Ambler and Logan, 2011) and used to determine the cathode coulombic efficiency (CE) based on the Coulombs produced during each cycle. The hydrogen production rate (L/L-d) was calculated by normalizing the volume of H_2 produced for the overall MEC reactor volume, which was 3.2 mL for the 9 cm^2 MEC and 35 mL for the 100 mL MEC. The anode coulombic efficiency was calculated based on the Coulombs produced and the chemical oxygen demand (COD) consumed (Choi et al., 2024). The COD was measured at each cycle. All measurements, including H2, and COD, were analyzed in at least duplicate (Table S1 and S3). Energy efficiency was calculated according to the previous studies (Izadi et al., 2025; Logan et al., 2006). As the bicarbonate concentration was not directly available, especially for real wastewater, it was estimated from the COD removal efficiency under the assumption that all bicarbonate originated from acetate oxidation.

3. Results and discussion

3.1. Impact of scaling up on the electrochemical performance of MECs

The 100 cm^2 and 9 cm^2 MECs produced similar current densities and hydrogen production rates (HPRs) when fed 50 mM PBS media with sodium acetate (2 g/L for 9 cm^2 and 5 g/L for 100 cm^2) following initial acclimation (Figure 2). Both 100 cm^2 and 9 cm^2 cells were successfully inoculated with effluent from other bioelectrochemical systems, and positive current was generated within 5 days of inoculation at V_{app} = –0.6 V (Figure S5). The 100 cm^2 reactor required a longer startup period of 5 days compared to the 9 cm^2 cells (2 days), likely due to the slower biofilm maturation over a larger electrode surface (V. H. Tran et al., 2022).

The 9 cm^2 cells achieved a maximum current density of 25.1 ± 2.7 A/m^2 at V_{app} of –1.1 V, while the 100 cm^2 cell reached a slightly lower maximum current density of 21.7 ± 1.1 A/m^2 at an applied voltage of –1.2 V. The current density in the larger MEC was 15.7% lower than that obtained in the 9 cm^2 cells and required a more negative applied voltage to be produced. This was due to the higher internal resistance (R_{int}) of the 100 cm^2 cell (19.7 ± 1.3 $m\Omega m^2$) compared to the smaller system (11.7 ± 0.5 $m\Omega m^2$) based on the linearization of the voltage over the polarization curve (See section 3.2.2). Notably, the performance of the 9 cm^2 cells was consistent with a previous study (23.7 ± 0.8 A/m^2) (Kim et al., 2025), indicating good reproducibility of performance in the serpentine-flow, zero-gap MEC design.

The CE of the MECs was comparable across different sizes, with both anodic and cathodic CE values larger than 70% (Figure 2). The cathodic CE of the 100 cm^2 cell remained consistently above 88% at all applied voltages and resulted in high hydrogen production rates from 19.9 (–0.7 V) to 69.3 L/L-d (–1.2 V), suggesting high efficacy in recovering hydrogen gas following scale-up. Previous studies reported a decrease in CE in scaled-up reactors due to changes in the electrochemical and hydrodynamic features (Brown et al., 2014). Here, the same HRTs were used for the small and large MECs, while the gas cathode chamber coupled with an optimized flow field design enabled consistent performance regardless of the reactor size. For example, at an applied voltage of –1.2 V, the larger MEC showed a HPR of 69.3 L/L-d, which was similar to that reported for the 9 cm^2 cells (HPR of 65.1 ± 9.3 L/L-d) under the same conditions. The maximum HPR (67.7 ± 2.4 L/L-d) of the 9 cm^2 cell was achieved at an applied voltage of –1.1 V, which was slightly lower than that previously reported in similar conditions (75.8 ± 4.1 L/L-d) due to a diminished CE (Kim et al., 2025). The anodic CE was comparable in the 100 cm^2 (>87%) and the 9 cm^2 (>72%), indicating that scaling up the electrode dimension by one order of magnitude did not affect electron recovery from organic substrate if a similar reactor architecture is used. The energy efficiency was comparable between the 9 cm^2 (91%) and 100 cm^2 MECs (102%) under synthetic wastewater conditions.

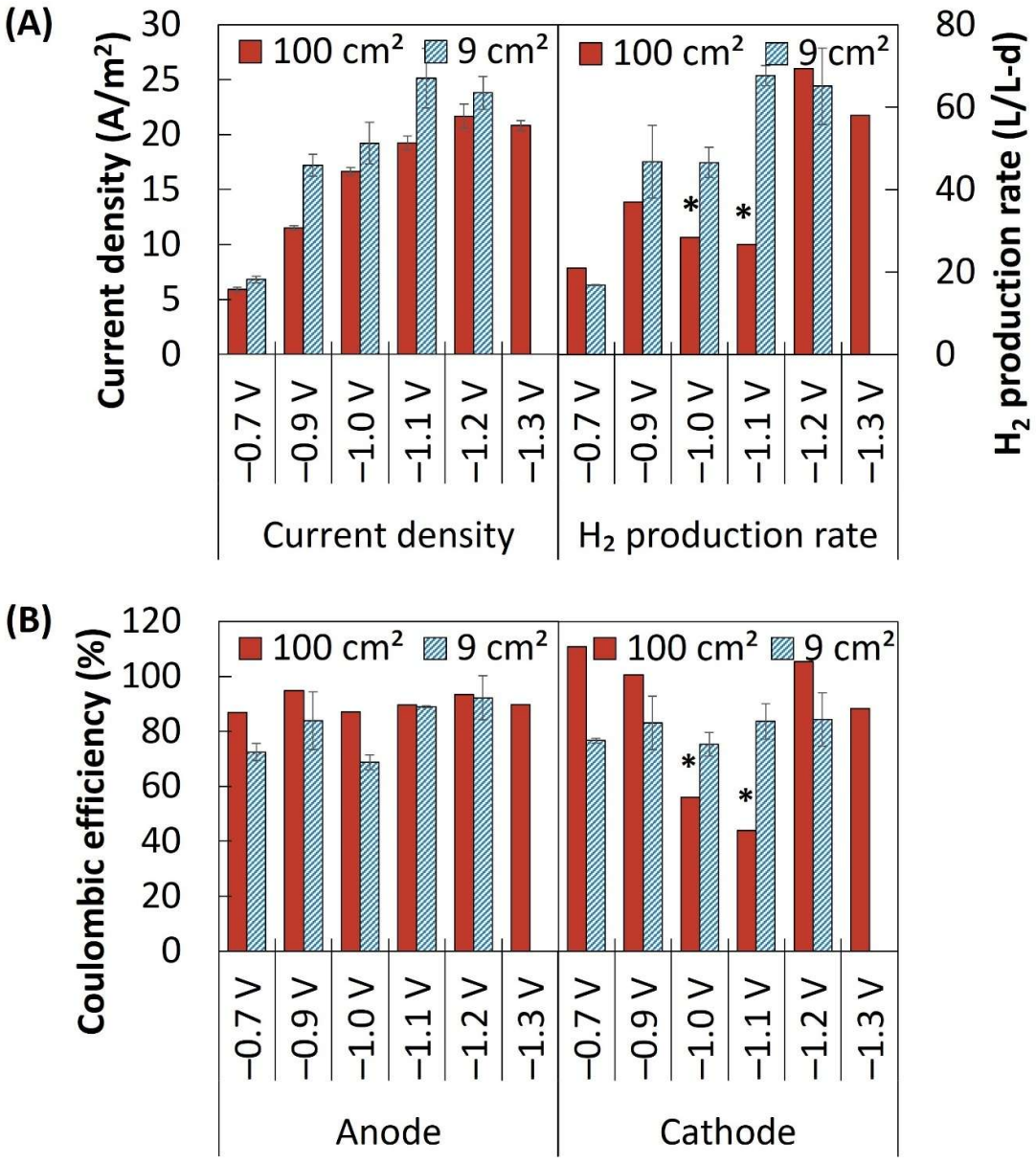

Figure 2. Performance of 100 cm^2 and 9 cm^2 MECs in terms of (A) current density and hydrogen production rate at each applied voltage. (B) Anodic and cathodic Coulombic efficiency at different applied voltages. Asterisks (*) indicate instances of hydrogen leakage from the gas bag.

3.2. Analysis of internal and electrode resistance in abiotic and biotic tests

3.2.1 Abiotic tests

Among the many components of a bioelectrochemical cell, the cathode is mostly affected by scaling up. Previous studies reported a significant increase in cathode resistance as the electrode dimensions were expanded due to a combination of a higher electrical resistance and electrode flooding caused by a larger water pressure (Rossi et al., 2019a). For example, a previous study reported an increase in cathode resistance during scale-up from 50 $m\Omega m^2$ at 7 cm^2, to 90 $m\Omega m^2$ at 33 cm^2, and to 300 $m\Omega m^2$ at 6200 cm^2 (Rossi et al., 2019b). To identify the most effective avenue for scaling up MEC cathodes without negatively impacting electrochemical performance, we evaluated cathode performance separated from anode in abiotic tests using the cathode MEAs coupled with a stainless-steel anode. These tests were used to assess membrane stability, understand water management, including the impact of water height on MEA permeability, and catalyst layer integrity. A thick membrane (130 µm) was needed to prevent anolyte leakage and maintain ionic continuity between the membrane and the NiMo cathode. A thinner 75 µm AEM that was previously used in the 9 cm^2 configuration resulted in frequent cathode detachment and significant water accumulation into the cathode gas chamber. Although membrane thickness can influence ion transport, its contribution to overall internal resistance in zero-gap MECs was reported to be minimal compared to anode and cathode resistances (Rossi et al., 2023a). For example, the ohmic resistance (75 µm) accounted for 8.8% (1.1 $m\Omega m^2$) of the internal resistance in a zero-gap configuration and changing membrane thickness did not affect performance (Kim et al., 2025). Here, the ohmic resistance was 3.6 $m\Omega m^2$ for the 100 cm^2 MEC and 1.2 $m\Omega m^2$ for the 9 cm^2 MEC with a 150 µm thickness, which is similar to the values previously reported.

Despite the different electrode areas, the abiotic tests revealed a similar cathode resistance between 9 cm^2 and 100 cm^2 electrodes. Cathode resistance (R_{cat}) in the 100 cm^2 was 4.6 ± 0.5 $m\Omega m^2$, comparable to 6.8 ± 0.5 $m\Omega m^2$ for the 9 cm^2 (Figure 3). Therefore, we demonstrated here that bench-scale cathode performance proportional to small systems can be achieved if electrode resistance, architecture, and water management are maintained in check. Proper membrane selection was key to avoid cathode flooding and a consequent decrease in performance.

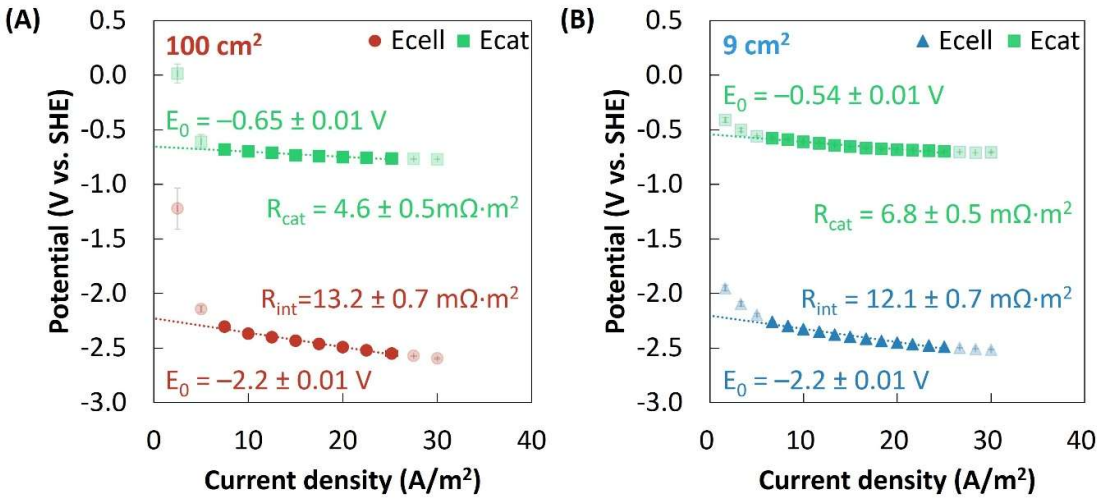

Figure 3. Cathodic potential as a function of current density in the abiotic (A) 100 cm^2 and (B) 9 cm^2 cell. Cathode performance was measured based on the pREs.

3.2.2 Biotic tests

The R_{int}, R_{an}, R_{cat}, and onset potential were assessed using the EPS analysis for the 100 cm^2 and 9 cm^2 MECs to quantify the impact of scale-up on electrochemical performance in the biotic tests. When compared to the 9 cm^2 cells (11.7 ± 0.5 $m\Omega m^2$), the R_{int} of the 100 cm^2 cell (19.7 ± 1.3 $m\Omega m^2$) was 68.4% higher (Figure 4A). The larger R_{int} of the 100 cm^2 MEC was primarily due to an increase in R_{an}, which was 16.2 ± 1.4 $m\Omega m^2$ in the 100 cm^2 cell, and only 10.0 ± 0.5 $m\Omega m^2$ in the 9 cm^2 cell. The increase in R_{an} was likely due to the development of mass-transport limitations in the 100 cm^2 system, which have been previously shown to dictate anode resistance due to the local electrode acidification (Torres et al., 2008) (Figure 4B). In contrast, R_{cat} remained similar after scaling-up, ranging from 4.5 ± 0.1 $m\Omega m^2$ (9 cm^2) to 2.8 ± 0.4 $m\Omega m^2$ (100 cm^2), consistent with the trend observed under the abiotic conditions (Figure 3).

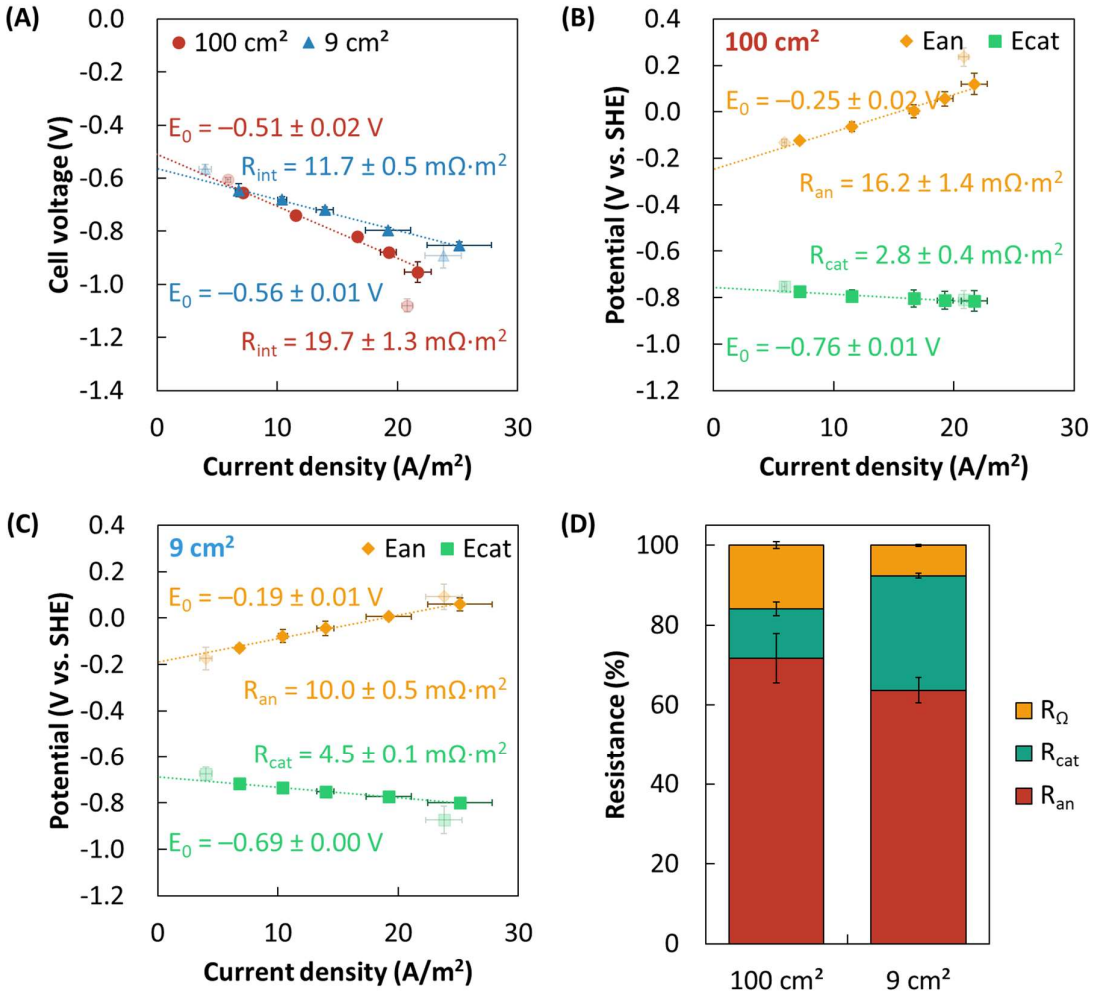

Figure 4. Polarization curves of (A) 100 cm^2 and 9 cm^2 MECs and corresponding anode and cathode performance for (B) 100 cm^2 cell and (C) 9 cm^2 cells. (D) Distribution of internal resistance components. Anode and cathode performance were measured based on the pREs. Error bars represent the standard deviation of the normalized resistance contributions, calculated by propagating the original standard deviations through percentage normalization.

The anode and cathode resistances obtained here were different than those we previously reported with a slightly different configuration. In our previous study, anode and cathode potentials were monitored in a circular flow field configuration (7 cm^2), using a reference electrode that was touching the end-plate side of the anode (Kim et al., 2025). In the previous study, a lower R_{an} (3.5 ± 1.2 $m\Omega m^2$) and a higher R_{cat} (9.3 ± 3.1 $m\Omega m^2$) were obtained, in contrast with the values observed here. This discrepancy in electrode resistance was likely due

to the different approaches used to monitor it, which could have led to the miscalculation of the ohmic resistance and overcorrection of the electrode potential, as previously reported (Logan et al., 2018). Using pREs placed between anode and cathode and in contact with the membrane is a more accurate method to monitor performance in zero-gap electrochemical systems (Hansen et al., 2022).

The R_{Ω} was measured via EIS, and increased from 1.2 mΩm^2 in the 9 cm^2 cells to 3.6 mΩm^2 in the 100 cm^2 cell, further contributing to the higher R_{int}. Overall, R_{an} was the most prominent contributor to the internal resistance for both 100 cm^2 cell (71.7%) and 9 cm^2 cell (63.7%) (Figure 4D). R_{cat} contributed by 12.4% in the 100 cm^2 cell and 28.7% in the 9 cm^2 cells, while the R_{Ω} accounted for 15.9% in the 100 cm^2 MEC and 7.6% in the 9 cm^2 cells. These results indicate a shift in resistance distribution during MEC scale-up and that components that primarily limit performance at small scale could have minimal impact in larger reactors. Therefore, monitoring resistance during scale up become critical. Electrochemical performance in terms of onset potential was compared between the abiotic and biotic tests. In biotic tests, the whole-cell onset potential was similar between the 9 cm^2 and 100 cm^2 MECs, suggesting that the scale-up did not affect the thermodynamic (excluding activation losses) of the electrochemical reactions at the electrodes (Figure 4A). For example, the whole-cell onset potential of 100 cm^2 was –0.51 ± 0.02 V, while that of 9 cm^2 cells was –0.56 ± 0.01 V.

Proper tightening of the screws was key to ensuring the zero-gap configuration by minimizing electrode spacing without limiting flow distribution (Figure S6). The internal resistance of the 100 cm^2 MEC was 27.0 ± 1.8 mΩm^2 with a spacing between the endplates larger than 3.5 mm. R_{int} decreased to 19.7 ± 1.3 mΩm^2 with a smaller spacing of 3.5 mm, and did not change at smaller distances. Both anodic (R_{an}) (21.4 ± 3.9 mΩm^2) and cathodic resistances R_{cat} (6.4 ± 2.3 mΩm^2) were substantially higher with larger spacing. The improvement in assembly quality was largely attributed to tight and uniform screwing, which ensured consistent electrical contact and optimized mass transport across the cell. These observations highlight the importance of precise assembly in minimizing internal resistance in large-scale zero-gap MECs.

3.3. Impact of hydrodynamic features on MEC scale up

The large anode resistance observed in 100 cm^2 MEC indicated that a mass transport-limited

regime was likely limiting the MEC performance. The anode resistance consists of a charge transfer resistance, due to the kinetics of electron transfer between the electroactive bacteria and the electrode, and a diffusion resistance, due to the accumulation of protons near the anode surface (Rossi et al., 2020; Sleutels et al., 2009b). To minimize diffusion resistance, lower hydraulic retention times were tested in the 100 cm^2 MEC. Experimental conditions were set to match the equivalent hydraulic retention times (1.08 min, 0.54 min, 0.36 min, 0.27 min, and 0.22 min) used in a prior study for the 9 cm^2 MEC, enabling a direct comparison of hydrodynamic and mass transport effects across scales under consistent operating conditions. The initial retention time was 0.36 min, which was selected as a baseline operating condition to maintain consistency with tests conducted on the 9 cm^2 in a previous study (Kim et al., 2025), while minimizing pumping energy requirements. Operation at an HRT of 0.36 min produced a current density of 20.9 ± 0.3 A/m^2 (Figure 5A). As the retention time decreased to 0.27 min and then to 0.22 min, the average current density increased to 22.8 ± 0.3 A/m^2 and to 23.8 ± 0.2 A/m^2 (Figure 5B). These increases in current density with decreasing retention time were likely due to the improvement of anolyte flow and enhanced mass transport at the bioanode. This could be attributed to the enhanced removal of stagnant liquid at higher flow rates, which likely improves mass transfer efficiency (Hernández-García et al., 2020; Lewis and Borole, 2016).

Following the conclusion of this experiment, when the retention time was returned to 0.36 min, the current density remained high at 23.8 ± 0.2 A/m^2. This might be attributed to the larger shear at high flow rate, which likely removed clogs and diminished biofilm thickness (Moß et al., 2020a; Moß et al., 2020b). Increasing the retention time from 0.36 min to 0.54 min and then to 1.08 min caused a notable decline in the current density, which dropped to 21.4 ± 0.3 A/m^2 and 17.1 ± 0.5 A/m^2 (Figure 5A). This reduction may be attributed to the limited substrate availability and accumulation of protons at the biofilm interface due to lower flow. Compared to the baseline (20.9 A/m^2) at 0.36 min retention time, current density decreased by 18.3% at 1.08 min and increased by 13.6% at 0.22 min.

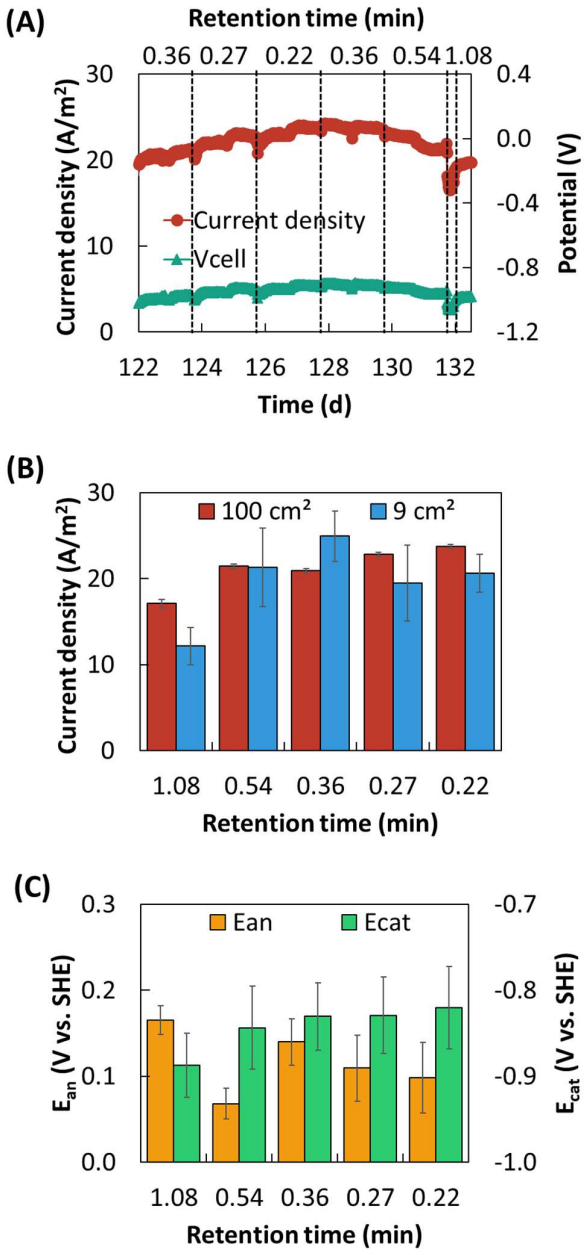

Figure 5. (A) Impact of retention times on current density and cell voltage (V_{cell}) in the 100 cm^2 MEC. (B) Comparison of current density at different retention times in 100 cm^2 and 9 cm^2 MECs. (C) Impact of flow rate on Ean and Ecat in the 100 cm^2 cell. Data for 9 cm^2 MECs were obtained from our previous study (Kim et al., 2025). Anode and cathode potentials were measured based on the pseudo-reference electrodes (pRE) positioned inside the cell.

To further examine the impact of the electrolyte distribution on the electrode

performance, E_{an} and E_{cat} were continuously monitored at each retention time (Figure 5C and Figure S7). While changes in flow rate had little impact on E_{cat}, there was a substantial impact on E_{an}. For example, increasing the retention time from 0.36 min to 1.08 min increased E_{an} by 18.2% and E_{cat} by only 6.9%. Conversely, decreasing the retention time from 0.22 min lowered E_{an} by 29.7%, while E_{cat} changed by less than 1.5%. These findings indicate that anode performance was more sensitive to flow conditions than the cathode, reinforcing the importance of optimizing anolyte distribution in scaled-up MECs.

The relative change in current density with varying retention times was substantially less pronounced in the 100 cm² MEC compared to the 9 cm² MEC, with a variation range of 39% versus 105% (Figure 5B). This indicates that the 100 cm² cell exhibited greater robustness under variable hydraulic conditions. Flow contour simulations further support this interpretation (Figure 6). The multiple-channel serpentine configuration in the 100 cm^2 cell promoted lower pressure drops across the large electrode area, in contrast to the single-channel 9 cm^2 MEC (Crandall et al., 2024). Comparison of the coefficient of variation values between the 9 cm^2 and 100 cm^2 cells revealed that the design of the 100 cm^2 cell showed better flow velocity uniformness, which translated into lower current density variance at varying retention times (Figure S8). For example, the coefficient of variation value of the 100 cm^2 MEC was 1.0, while that of the 9 cm^2 cell was 1.7 at a retention time of 0.36 min. These findings highlight the importance of ensuring that flow distribution is maintained in check during scale up. The serpentine flow field used here not only improved electrochemical efficiency but also contributed to operational robustness, a key requirement for scale-up and field deployment.

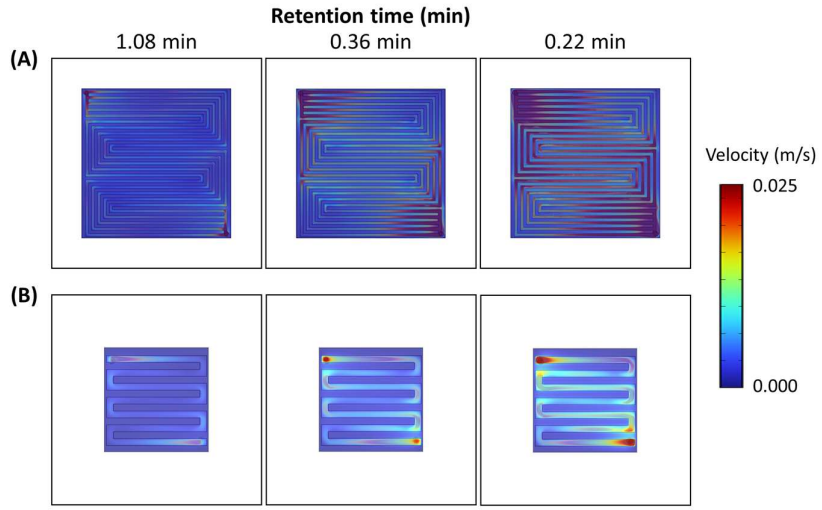

Figure 6. The flow velocity contours in the anode chamber of (A) 100 cm^2 MEC and (B) 9 cm^2 MEC. For visual comparison, the 9 cm^2 cell was scaled to match the dimensions of the 100 cm^2 cell.

3.4. Impact of scale-up on microbial ecology characteristics

A total of 645,117 non-chimeric, quality-filtered reads were obtained from the nine samples from the 100 cm^2 cell and the four samples from the 9 cm^2 MECs after operating with synthetic wastewater. The samples were clustered into 213 OTUs, resulting in libraries consisting of 623,587 bacterial reads, corresponding to 96.7% of the total, and 21,530 archaeal reads, accounting for 3.3% of the total reads. These reads identified 199 bacterial and 14 archaeal OTUs. The bacterial communities were more diverse than archaeal communities, which accounted for only 3% of the overall genera and were dominated by hydrogenotrophic *Methanobacterium* (44.1–95.3%) and *Methanobrevibacter* (4.3–56.0%), together accounting for 98.5–100% of the archaeal reads. Given their relatively low abundance, the impact of hydrogenotrophic methanogens on hydrogen consumption was likely limited, thereby minimal competition with anodic processes and supporting higher anodic CE.

A wide range of bacterial genera was identified in both the 100 cm^2 and 9 cm^2 MECs, although a substantial proportion of sequences were classified into the 'Others' category. (Figure 7). *Geobacter*, a well-known electroactive genus, was most dominant in the 100 cm^2 cell, with a relative abundance ranging from 31.3% to 61.7%. Among fermentative bacteria, *Parabacteroides* was the second most abundant genus (22.0–46.0%), capable of producing

volatile fatty acids as fermentation end-products (Cha et al., 2024; Liu et al., 2016). *Aminiphilus*, a fermenter of amino acids, was also present at 2.8–5.5% relative abundance. Interestingly, *Geobacter* showed a strong negative correlation with *Parabacteroides* and *Wolinella*, indicating potential competition under substrate-limited conditions caused by faster substrate depletion (Figure S9).

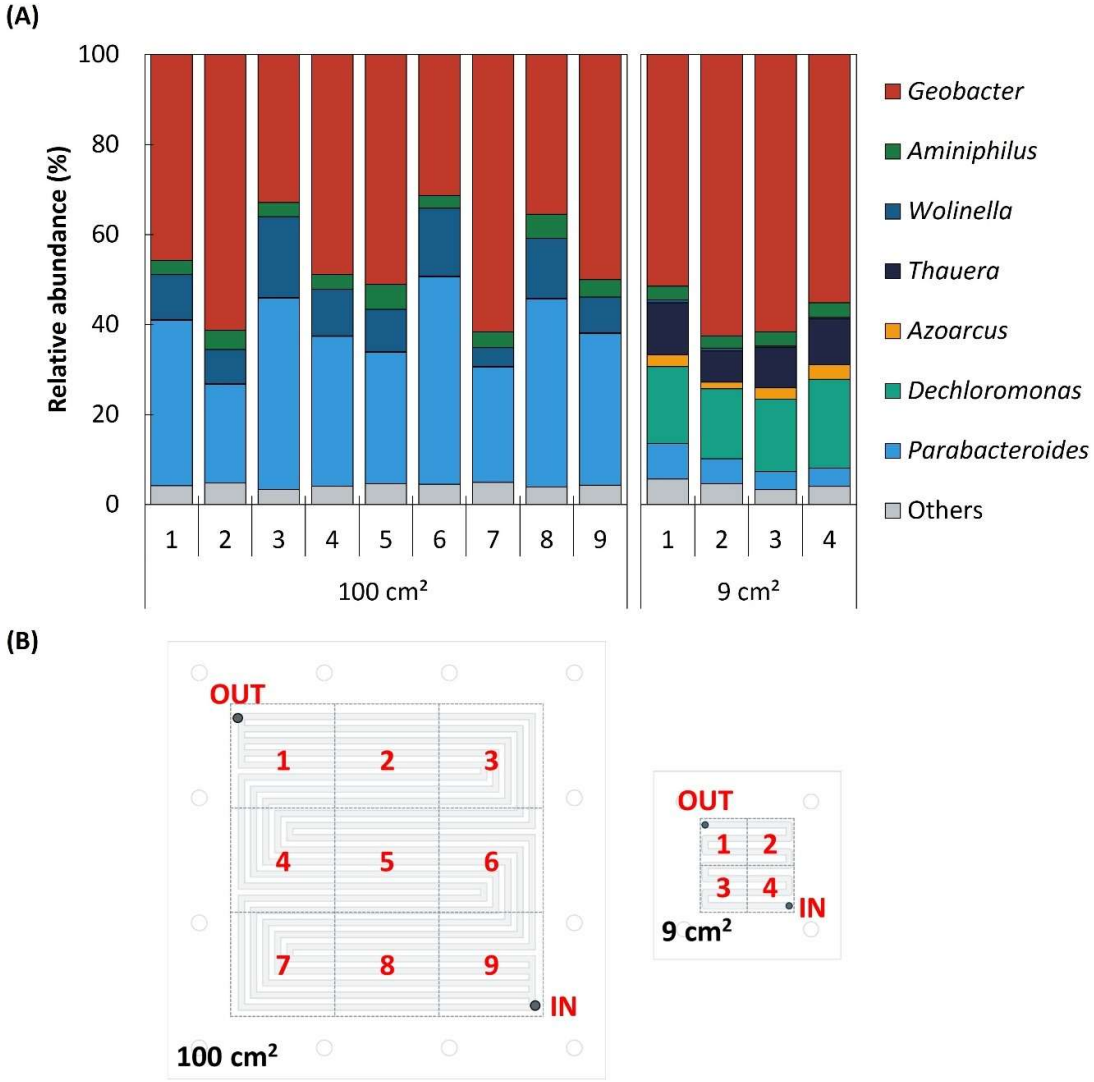

Figure 7. (A) Genus-level bacterial community compositions in anodic biofilms. Bacterial genera with a relative abundance less than 3% across all samples were grouped as "Others". (B) Position of the sampling points in the 9 cm^2 and 100 cm^2 MECs. "In" and "Out" indicate the flow path.

Similar to the 100 cm^2 cell, *Geobacter* was also the dominant genus in the 9 cm^2 cell, with a relative abundance ranging between 51.6–62.6%, and *Aminiphilus* was present at comparable levels (2.7–3.2%). Other fermentative bacteria and electroactive taxa coexisted as in the larger MEC. However, denitrifying bacteria such as *Thauera* and *Dechloromonas* were relatively more abundant in the smaller system, collectively comprising 22.5–30.0% of the bacterial community. *Dechloromonas*, a nitrate-reducing, iron-oxidizing bacterium with anode-respiring capability (Guo et al., 2024; Li et al., 2021), was the second most abundant genus (15.6–19.7%). In both MEC sizes, non-electroactive bacteria, such as *Parabacteroides*, may have contributed to reducing anodic CE by competing for acetate in the anolyte (Li et al., 2021), and all identified genera are commonly found in microbial electrochemical systems.

All alpha-diversity metrics (Shannon, Simpson, Chao-1, and ACE) exhibited overlapping ranges (Table S2). Although the 9 cm^2 cell showed a slight tendency toward higher richness and diversity, these differences were minor. For example, the Shannon index ranged from 1.5 to 1.7 in the 100 cm^2 cell and from 1.6 to 2.1 in the 9 cm^2 cell. Therefore, the microbial communities in the 100 cm^2 and 9 cm^2 cells were broadly similar, with only modest variations in richness.

3.4. Operation with real anaerobic digester effluent

Unamended single-stage anaerobic digestor was used in the 100 cm^2 MEC to evaluate performance using real waste streams. The anaerobic digester effluent had a total COD of 0.7 ± 0.1 g COD/L (pH 6.7; conductivity 1.0 mS/cm). The maximum current density reached 5.6 ± 0.6 A/m^2 at an applied voltage of –1.2 V, which was 56% higher compared to the 3.6 ± 0.2 A/m^2 previously obtained in the 9 cm^2 cell using the same media with similar composition (Figure 8A) (Kim et al., 2025). The maximum hydrogen production rate was also higher in the 100 cm^2 cell, reaching 16.3 L/L-d compared to 8.3 L/L-d for 9 cm^2 (Kim et al., 2025). The R_{int} of the 100 cm^2 cell with 20 µm filtered wastewater was 71.5 ± 0.4 $m\Omega m^2$, which was 31% lower than that of 9 cm^2 cell with 1.5 µm filtered wastewater (102.9 ± 9.1 $m\Omega m^2$) (Figure 8B). The lower buffer capacity of real wastewater caused a decrease in the maximum current density of the MEC and a consequently lower hydrogen production rate, in agreement with the results obtained in previous studies (Du et al., 2026; Wang et al., 2025). Coulombic efficiencies during this period showed >93% in both the anode and cathode (Figure 8C), while the maximum COD

removal efficiency was approximately 22% and increased as the current density increased, in line with previous studies (Table S3) (Zhang et al., 2015). The energy efficiency was 83% regardless of the scale. Therefore, the large MEC produced slightly larger performance compared to the 9 cm^2 reactor when operated with real waste streams. Notably, the current density reported here is one of the largest reported to date with unamended domestic wastewater.

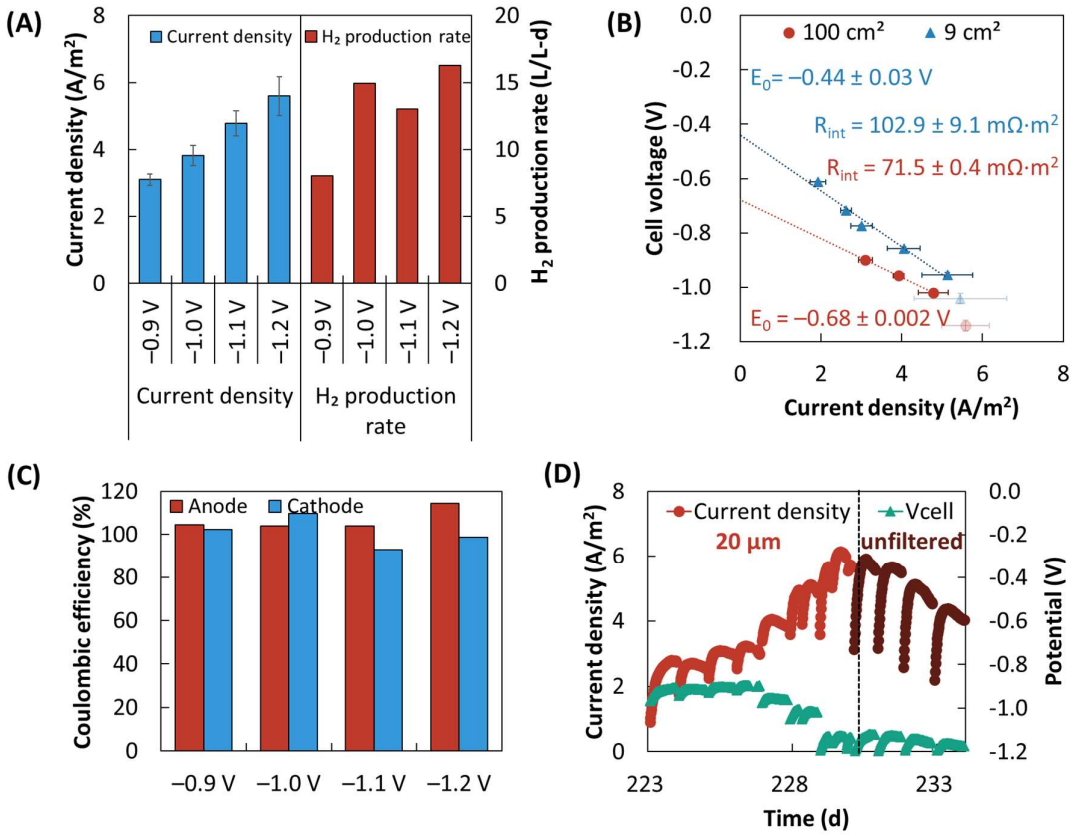

Figure 8. Performance of the 100 cm^2 MEC fed wastewater from a single-stage anaerobic digestion. (A) Current density and hydrogen production rate. (B) Polarization curve with different applied voltage. (C) Coulombic efficiencies. (D) Long-term performance of the 100 cm^2 MEC fed wastewater from a single-stage anaerobic digestion (20 µm filtered or unfiltered).

To further evaluate robustness of the MEC fed real wastewater, the 100 cm^2 MEC was operated with unfiltered effluent for 4 additional days (Figure 8D). During this period, the average current density was 4.9 ± 0.8 A/m^2, but it gradually declined over time. Coulombic efficiencies remained >89%, showing that electron loss was not responsible for the reduced current

560 density. Operation could not be extended beyond 4 days since the MEC consumed 4 L of
561 wastewater per day. Clogging was initially considered as a possible reason for the decline in
562 performance. However, there was no accumulation of solids in the anode chamber based on
563 visual inspection after disassembly and based on the analysis of totals suspended solids in the
564 inlet and in the outlet of the MEC (Figure S10A). White solids were found on membrane facing
565 the anode chamber, likely due to the precipitation of metal carbonates due to the
566 development of a pH gradient between the anode and cathode chambers caused by the
567 wastewater's low buffering capacity (175 mg/L as $CaCO_3$; 0.27 mmol/pH; from initial pH to pH
568 5.5) (Figure S10B). These precipitates may contribute to impairing ion transport and increasing
569 internal resistance by blocking membrane pores and reducing the effective electrode surface
570 area (Luo et al., 2012).
571
572 *3.6. Outlook and perspectives*
573 In this paper, we established a framework based on electrochemical, hydrodynamic, and
574 microbial ecology features to characterize and control the performance of MECs during scale-
575 up. Our findings demonstrate that it is feasible to increase electrode size and reactor
576 dimension by one order of magnitude without negatively affecting performance by controlling
577 and optimizing reactor configuration and flow field design. The similar internal resistance with
578 one order of magnitude larger electrode size enabled comparable current density and
579 hydrogen production rates at different scales. In addition, the use of pseudo-reference
580 electrodes allowed us to monitor the individual electrode performance and pinpoint major
581 limitations of larger MECs, aiding in the development of operational strategies to overcome
582 these barriers, such as maintaining a high flow rate to limit anode acidification. Future studies
583 are needed to clarify whether performance can be maintained in MECs with electrode areas
584 beyond 100 cm^2. Following the identification of the optimal electrode size, additional efforts
585 will be needed to develop cell stacks and manage voltage, current, and hydrogen production
586 in the assembly.
587 Other studies reported substantial increases in internal resistance during scale-up, leading
588 to subpar performance in larger reactors. For example, a single-chamber system with an
589 electrode area of 90 cm^2, similar to that used here, exhibited an internal resistance of 432
590 $m\Omega m^2$ with a wastewater electrolyte, approximately 6 times higher than that obtained here

with wastewater (71.5 ± 0.4 $m\Omega m^2$) (Escapa et al., 2012). The small internal resistance of the MEC used in this study was due to the zero-gap configuration coupled with a gas chamber at the cathode. By minimizing electrode distance, the resistance due to solution conductivity was reduced, while a small spacing between anode and cathode in the absence of a liquid catholyte facilitated the transport of hydroxide ions from the cathode to the anode, minimizing R_{an} by limiting local acidification of the biofilm. Zero-gap MECs are more prone to clogging when fed real waste streams, but we previously demonstrated that the serpentine flow path configuration used here enabled operation with electrolytes containing a large concentration of suspended solids (Kim et al., 2025).

In the majority of the other double-chamber systems in which a liquid catholyte with salt was used, the internal resistance was systematically larger than that reported here. For example, 192 $m\Omega m^2$ were reported in an MEC with electrode areas of 250 cm^2 and an AEM using a synthetic media compared to 19.7 ± 1.3 $m\Omega m^2$ reported in this study. (Sleutels et al., 2009a). In one previous study, a current density similar to the one reported here was obtained with 100 cm^2 electrodes, but performance could not be maintained and rapidly decreased over time (Jeremiasse et al., 2010). The two-chamber MEC equipped with a 100 cm^2 anode, AEM, and a Ni foam cathode delivered current densities of 22.8 ± 0.1 A/m^2 and HPR of 50.0 L/L-d at an E_{cell} of –0.9 V with an internal resistance of 16.4 ± 0.4 $m\Omega m^2$ (Jeremiasse et al., 2010), according to the previous study. This system operated with 100 mM PBS as anolyte and 0.1 M KCl as catholyte, at a flow rate of 120 mL/min. High buffer capacities allow for better management of the pH near the electrodes and minimize anode resistance (Rossi et al., 2020). Our 100 cm^2 MEC with AEM and gas cathode chamber delivered 21.7 ± 1.1 A/m^2 with a PBS concentration of 50 mM, producing a slightly higher internal resistance of 20.4 ± 1.0 $m\Omega m^2$ and a much larger (32%) HPR of 69.3 L/L-d due to the more compact design (Figure 9A). With 100 mM PBS, our system achieved a higher current density of 22.7 ± 0.14 A/m^2 and an HPR of 80.0 L/L-d. Despite the similar maximum performance, our MEC was operated for more than six months without an apparent decrease in performance compared to a rapid maximum current decrease previously reported. In 18 days, a current density decrease of 0.5 A/m^2 per day was reported in the previous study due to electrode scaling and membrane degradation from high pH gradient, compared to no change in the present work (Figure 9B) (Jeremiasse et al., 2010). High performance stability in our configuration was likely due to the use of a gas

chamber at the cathode, which enabled the selective transport of hydroxide ions, rather than chloride ions, from cathode to anode (Rohbohm and Angenent, 2025; Rossi et al., 2023b). These results highlight the advantages of a gas chamber at the cathode in a zero-gap configuration, which enables better pH management and therefore high performance and long-term stability even under low buffer conditions, supporting the potential of this design as an economically viable configuration for scaled-up MECs.

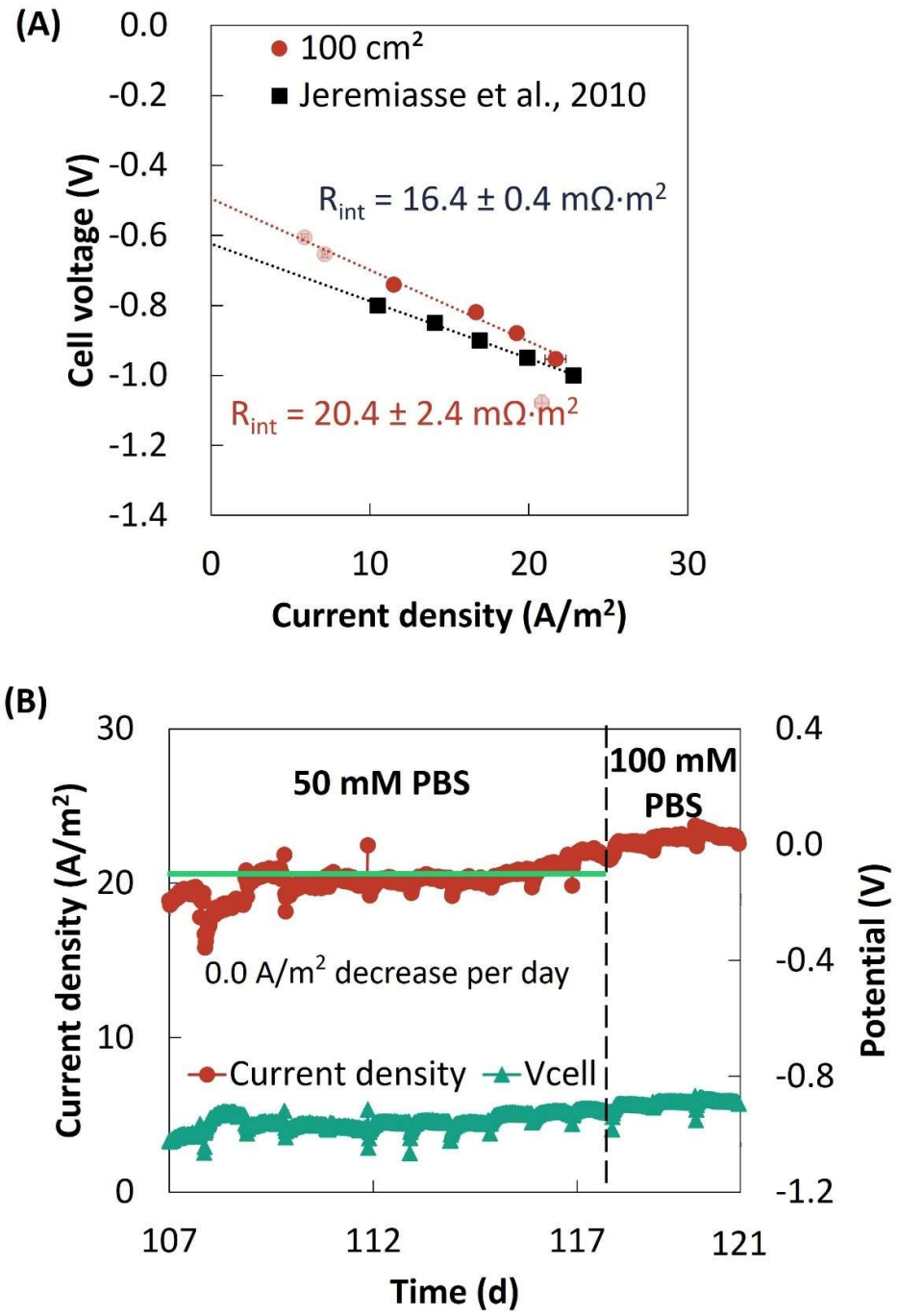

628

629 **Figure 9**. (A) Polarization curves of this study (50 mM PBS) and Jeremiasse et al. (100 mM PBS).

630 (B) Current density and cell voltage (V_{cell}) over time during long-term operation with synthetic

631 wastewater containing 5 g/L sodium acetate.

632

The hydrogen cost calculated from long-term operation in the 100 cm^2 MEC was 1.7 $/kg$H_2$ with synthetic wastewater and 2.2 $/kg$H_2$ with the anaerobic digester effluent, which is lower than that of typical abiotic water electrolyzers . For example, a proton exchange membrane (PEM) water electrolyzer operating with pure distilled water at 30–55 °C achieved 5.9 $/kg$H_2$ (Abdulrahman et al., 2025). Alkaline water electrolysis with 30 wt% KOH at 80 °C achieved 4.1 $/kg$H_2$ (Liao et al., 2024). These cost estimates are based only on electricity consumption; they do not include other balance of plants operation, which will likely increase the expenditure, but also do not account for additional cost benefits due to the removal of organic contaminants from liquid waste streams in MECs. Considering that the current cost for hydrogen production from natural gas is between \$1.5/kgH_2 and \$2.5/kgH_2 (Curcio, 2025), MECs offer not only a sustainable pathway for hydrogen generation compared to conventional approaches, but also substantial economic benefits.

4. Conclusion

This study demonstrated how electrochemistry, hydrodynamic, and microbial ecology features change during the scale-up of MECs. Controlling each of these parameters allowed us to maintain current density and hydrogen production rates while scaling up the electrode area by an order of magnitude from 9 cm^2 to 100 cm^2. By systematically tracking internal resistance, onset potential, and electrode potentials using advanced four-electrode monitoring, we identified how scaling up from 9 cm^2 to 100 cm^2 influenced electrochemical characteristics and addressed these limitations through targeted optimization. Despite a 68.4% higher internal resistance in the scaled-up system, the bench-scale MEC achieved a high hydrogen production rate of 69.3 L/L-d and a stable current density of 21.7 ± 1.1 A/m^2 at an applied voltage of –1.2 V in 50 mM PBS, exceeding prior studies with similar electrode areas. Shorter retention time had a positive effect on current generation, while longer retention times significantly decreased current production due to the establishment of mass-transfer limitations at the anode. The microbial community structure was broadly similar across MEC scales, with only minor variations associated with the electrode dimension. . *Geobacter* was the dominant genus in both systems.. Overall, these findings underscore the critical role of real-time electrochemical monitoring to guide the design and operation of scaled up MECs, providing a pathway toward practical, efficient, and economically viable MEC systems for

hydrogen production from liquid waste streams.

Acknowledgement

RR acknowledge support from the US Department of Energy award DE-EE0009623 and Johns Hopkins University.

Literature cited:

Abdulrahman, A.M., Abas, A., Abdullah, M.Z., Mahdi, M.M. and Oohayyid, T. 2025. Impact of elevated water temperature on hydrogen production in PEM systems using KOH catalysts. Int. J. Hydrogen Energy 157, 150439.

Ambler, J.R. and Logan, B.E. 2011. Evaluation of stainless steel cathodes and a bicarbonate buffer for hydrogen production in microbial electrolysis cells using a new method for measuring gas production. Int. J. Hydrogen Energy 36(1), 160-166.

Brown, R.K., Harnisch, F., Wirth, S., Wahlandt, H., Dockhorn, T., Dichtl, N. and Schröder, U. 2014. Evaluating the effects of scaling up on the performance of bioelectrochemical systems using a technical scale microbial electrolysis cell. Bioresour. Technol. 163, 206-213.

Cario, B.P., Rossi, R., Kim, K.-Y. and Logan, B.E. 2019. Applying the electrode potential slope method as a tool to quantitatively evaluate the performance of individual microbial electrolysis cell components. Bioresour. Technol. 287, 121418.

Cha, J., Choi, Y., Park, H., Kim, D., Baek, G. and Lee, C. 2024. Combining pre-fermentation and microbial electrolysis for efficient hydrogen production from food wastewater. Process Saf. Environ. Prot. 187, 1471-1480.

Cheng, S., Ye, Y., Ding, W. and Pan, B. 2014. Enhancing power generation of scale-up microbial fuel cells by optimizing the leading-out terminal of anode. J. Power Sources 248, 931-938.

Choi, Y., Kim, D., Choi, H., Cha, J., Baek, G. and Lee, C. 2024. Comparative study of exoelectrogenic utilization preferences and hydrogen conversion among major fermentation products in microbial electrolysis cells. Bioresour. Technol. 393, 130032.

Crandall, B.S., Ko, B.H., Overa, S., Cherniack, L., Lee, A., Minnie, I. and Jiao, F. 2024. Kilowatt-scale tandem CO_2 electrolysis for enhanced acetate and ethylene production. Nat. Chem. Eng. 1(6), 421-429.

Curcio, E. 2025. Techno-economic analysis of hydrogen production: Costs, policies, and scalability in the transition to net-zero. Int. J. Hydrogen Energy 128, 473-487.

Du, H., Kim, D. and Rossi, R. 2026. Zero-gap microbial electrolysis cells for efficient hydrogen production from real liquid waste streams. Bioresour. Technol. 443, 133830.

Edgar, R.C.J.B. 2010. Search and clustering orders of magnitude faster than BLAST. Bioinformatics 26(19), 2460-2461.

Edgar, R.C.J.B. 2016. UNOISE2: improved error-correction for Illumina 16S and ITS amplicon sequencing. BioRxiv. 081257.

Escapa, A., Gil-Carrera, L., García, V. and Morán, A. 2012. Performance of a continuous flow microbial electrolysis cell (MEC) fed with domestic wastewater. Bioresour. Technol. 117, 55-62.

Fan, Y., Sharbrough, E. and Liu, H. 2008. Quantification of the Internal Resistance Distribution of Microbial Fuel Cells. Environ. Sci. Technol. 42(21), 8101-8107.

Feng, Y., Yang, Q., Wang, X. and Logan, B.E. 2010. Treatment of carbon fiber brush anodes for improving power generation in air–cathode microbial fuel cells. J. Power Sources 195(7), 1841-1844.

Gao, L., Liu, W., Cui, M., Zhu, Y., Wang, L., Wang, A. and Huang, C. 2021. Enhanced methane production in an up-flow microbial electrolysis assisted reactors: Hydrodynamics characteristics and electron balance under different spatial distributions of bioelectrodes. Water Res. 191, 116813.

Ghorui, U.K., Sivaguru, G., Teja, U.B., M, A., Ramakrishna, S., Ghosh, S., Dalapati, G.K. and Chakrabortty, S. 2024. Anion-Exchange Membrane Water Electrolyzers for Green Hydrogen Generation: Advancement and Challenges for Industrial Application. ACS Appl. Energy Mater. 7(18), 7649-7676.

Guo, M., Wei, S., Guo, M., Li, M., Qi, X., Wang, Y. and Jia, X. 2024. Potential mechanisms of propionate degradation and methanogenesis in anaerobic digestion coupled with microbial electrolysis cell system: Importance of biocathode. Bioresour. Technol. 400, 130695.

Hammer, Ø. and Harper, D.A.J.P.e. 2001. Past: paleontological statistics software package for educaton and data anlysis. Palaeontol. Electron. 4(1), 1.

Hansen, K.U., Cherniack, L.H. and Jiao, F. 2022. Voltage Loss Diagnosis in CO2 Electrolyzers Using Five-Electrode Technique. ACS Energy Lett. 7(12), 4504-4511.

Hernández-García, K.M., Cercado, B., Rivero, E.P. and Rivera, F.F. 2020. Theoretical and experimental evaluation of the potential-current distribution and the recirculation flow rate effect in the performance of a porous electrode microbial electrolysis cell (MEC). Fuel 279, 118463.

Izadi, P., Korth, B. and Harnisch, F. 2025. On assessing the energy efficiency of bioelectrochemical systems for cathodic synthesis and remediation. J. Power Sources 652, 237631.

Jeremiasse, A.W., Hamelers, H.V., Saakes, M. and Buisman, C.J.J.I.J.o.H.E. 2010. Ni foam cathode enables high volumetric H2 production in a microbial electrolysis cell. 35(23), 12716-12723.

Jiang, J., Du, L., Si, B., Kawale, H.D., Wang, Z., Summers, S., Lopez-Ruiz, J.A., Li, S., Zhang, Y. and Ren, Z.J. 2025. Pilot microbial electrolysis cell closes the hydrogen loop for hydrothermal wet waste conversion to jet fuel. Water Res. 268, 122644.

Kim, D., Yun, N., Du, H., Moreno Jimenez, D.A. and Rossi, R. 2025. Flow field design for zero-gap microbial electrolysis cells using synthetic and real wastewater. J. Power Sources 630, 236077.

Kim, M.-H., Nguyen, V.T., Im, S., Jung, Y., Choi, S.-R. and Kim, B.-J. 2021. Experimental Validation of Flow Uniformity Improvement by a Perforated Plate in the Heat Exchanger of SFR Steam Generator. Energies 14(18), 5846.

741 Lee, H.-S., Xin, W., Katakojwala, R., Venkata Mohan, S. and Tabish, N.M.D. 2022. Microbial
742 electrolysis cells for the production of biohydrogen in dark fermentation – A review.
743 Bioresour. Technol. 363, 127934.
744 Lewis, A.J. and Borole, A.P. 2016. Understanding the impact of flow rate and recycle on the
745 conversion of a complex biorefinery stream using a flow-through microbial electrolysis cell.
746 Biochem. Eng. J. 116, 95-104.
747 Li, T. 2025. Study on the parameters of DLC coating preparation process based on COMSOL.
748 Journal of Physics: Conference Series 2951(1), 012069.
749 Li, Z.-L., Zhu, Z.-L., Lin, X.-Q., Chen, F., Li, X., Liang, B., Huang, C., Zhang, Y.-M., Sun, K., Zhou, A.-N.
750 and Wang, A.-J. 2021. Microbial fuel cell-upflow biofilter coupling system for deep
751 denitrification and power recovery: Efficiencies, bacterial succession and interactions. Environ.
752 Res. 196, 110331.
753 Liao, Y., Deng, G., Ding, L. and Wang, H. 2024. A thin and flexible composite membrane with low
754 area resistance and high bubble point pressure for advanced alkaline water electrolysis. J.
755 Membr. Sci. 689, 122182.
756 Liu, W., He, Z., Yang, C., Zhou, A., Guo, Z., Liang, B., Varrone, C. and Wang, A.-J. 2016. Microbial
757 network for waste activated sludge cascade utilization in an integrated system of microbial
758 electrolysis and anaerobic fermentation. Biotechnol. Biofuels 9(1), 83.
759 Logan, B.E., Hamelers, B., Rozendal, R., Schröder, U., Keller, J., Freguia, S., Aelterman, P., Verstraete, W.
760 and Rabaey, K. 2006. Microbial Fuel Cells: Methodology and Technology. Environ. Sci.
761 Technol. 40(17), 5181-5192.
762 Logan, B.E., Zikmund, E., Yang, W., Rossi, R., Kim, K.-Y., Saikaly, P.E. and Zhang, F. 2018. Impact of
763 Ohmic Resistance on Measured Electrode Potentials and Maximum Power Production in
764 Microbial Fuel Cells. Environ. Sci. Technol. 52(15), 8977-8985.
765 Luo, H., Xu, P., Jenkins, P.E. and Ren, Z. 2012. Ionic composition and transport mechanisms in
766 microbial desalination cells. J. Membr. Sci. 409-410, 16-23.
767 Moß, C., Behrens, A. and Schröder, U. 2020a. The Limits of Three-Dimensionality: Systematic
768 Assessment of Effective Anode Macrostructure Dimensions for Mixed-Culture Electroactive
769 Biofilms. ChemSusChem 13(3), 582-589.
770 Moß, C., Jarmatz, N., Hartig, D., Schnöing, L., Scholl, S. and Schröder, U. 2020b. Studying the
771 Impact of Wall Shear Stress on the Development and Performance of Electrochemically
772 Active Biofilms. Chempluschem 85(10), 2298-2307.
773 Park, J.E., Kang, S.Y., Oh, S.-H., Kim, J.K., Lim, M.S., Ahn, C.-Y., Cho, Y.-H. and Sung, Y.-E. 2019. High-
774 performance anion-exchange membrane water electrolysis. Electrochim. Acta 295, 99-106.
775 Rohbohm, N. and Angenent, L.T. 2025. A development study for liquid- and vapor-fed anode
776 zero-gap bioelectrolysis cells. iScience 28(7).
777 Rossi, R., Baek, G. and Logan, B.E. 2022. Vapor-Fed Cathode Microbial Electrolysis Cells with
778 Closely Spaced Electrodes Enables Greatly Improved Performance. Environ. Sci. Technol. 56(2),
779 1211-1220.

780 Rossi, R., Cario, B.P., Santoro, C., Yang, W., Saikaly, P.E. and Logan, B.E. 2019a. Evaluation of
781 Electrode and Solution Area-Based Resistances Enables Quantitative Comparisons of Factors
782 Impacting Microbial Fuel Cell Performance. Environ. Sci. Technol. 53(7), 3977-3986.
783 Rossi, R., Hall, D.M., Wang, X., Regan, J.M. and Logan, B.E. 2020. Quantifying the factors limiting
784 performance and rates in microbial fuel cells using the electrode potential slope analysis
785 combined with electrical impedance spectroscopy. Electrochim. Acta 348, 136330.
786 Rossi, R., Jones, D., Myung, J., Zikmund, E., Yang, W., Gallego, Y.A., Pant, D., Evans, P.J., Page, M.A.,
787 Cropek, D.M. and Logan, B.E. 2019b. Evaluating a multi-panel air cathode through
788 electrochemical and biotic tests. Water Res. 148, 51-59.
789 Rossi, R., Nicolas, J. and Logan, B.E. 2023a. Using nickel-molybdenum cathode catalysts for
790 efficient hydrogen gas production in microbial electrolysis cells. J. Power Sources 560,
791 232594.
792 Rossi, R., Taylor, R. and Logan, B.E. 2023b. Increasing the Electrolyte Salinity to Improve the
793 Performance of Anion Exchange Membrane Water Electrolyzers. ACS Sustainable Chemistry
794 & Engineering 11(23), 8573-8579.
795 San-Martín, M.I., Sotres, A., Alonso, R.M., Díaz-Marcos, J., Morán, A. and Escapa, A. 2019.
796 Assessing anodic microbial populations and membrane ageing in a pilot microbial
797 electrolysis cell. Int. J. Hydrogen Energy 44(32), 17304-17315.
798 Sauermoser, M., Kizilova, N., Pollet, B.G. and Kjelstrup, S.J.F.i.E.R. 2020. Flow field patterns for
799 proton exchange membrane fuel cells. Front. Energy Res., 8, 13.
800 Sleutels, T.H.J.A., Hamelers, H.V.M., Rozendal, R.A. and Buisman, C.J.N. 2009a. Ion transport
801 resistance in Microbial Electrolysis Cells with anion and cation exchange membranes. Int. J.
802 Hydrogen Energy 34(9), 3612-3620.
803 Sleutels, T.H.J.A., Lodder, R., Hamelers, H.V.M. and Buisman, C.J.N. 2009b. Improved performance
804 of porous bio-anodes in microbial electrolysis cells by enhancing mass and charge transport.
805 Int. J. Hydrogen Energy 34(24), 9655-9661.
806 Torres, C.I., Kato Marcus, A. and Rittmann, B.E. 2008. Proton transport inside the biofilm limits
807 electrical current generation by anode-respiring bacteria. Biotechnol. Bioeng. 100(5), 872-
808 881.
809 V. H. Tran, H., Kim, E. and Jung, S.P. 2022. Anode biofilm maturation time, stable cell performance
810 time, and time-course electrochemistry in a single-chamber microbial fuel cell with a brush-
811 anode. J. Ind. Eng. Chem. 106, 269-278.
812 Wang, L., Linowski, K., Islam, M.Z., Harrison, H., Yu, C. and Liu, H. 2025. Efficient hydrogen
813 production from low-conductivity high-strength wastewater without buffer addition using
814 compact electrode assemblies in membraneless microbial electrolysis cells. Chem. Eng. J.
815 519, 165062.
816 Zhang, X., He, W., Ren, L., Stager, J., Evans, P.J. and Logan, B.E. 2015. COD removal characteristics
817 in air-cathode microbial fuel cells. Bioresour. Technol. 176, 23-31.
818